OceanDynamics manuscript No.
(will be inserted by the editor)

Numerical studies of flow over a sill: sensitivity of the non-hydrostatic effects to the grid size

Jarle Berntsen · Jiuxing Xing · Alan M. Davies

Received: date / Accepted: date

Abstract A non-hydrostatic terrain following model in cross sectional form is applied to study the processes in the lee of a sill in an idealized stratified fjord during super-critical tidal inflow. A sequence of numerical studies with horizontal grid sizes in the range from 100 m to 1.5625 m are performed. All experiments are repeated using both hydrostatic and non-hydrostatic versions of the model allowing a

---

Jarle Berntsen

Department of Mathematics, University of Bergen, Johannes Brunsgate 12, N-5008 Bergen, Norway

Tlf.: 47-55584854

Fax: 47-55589672

E-mail: jarle.berntsen@math.uib.no

Jiuxing Xing

Proudman Oceanographic Laboratory, Joseph Proudman Building, 6 Brownlow Street, Liverpool L3 5DA, UK

Alan M. Davies

Proudman Oceanographic Laboratory, Joseph Proudman Building, 6 Brownlow Street, Liverpool L3 5DA, UK

systematic study of possible non-hydrostatic pressure effects and also of the sensitivity of these effects to the horizontal grid size.

The length scales and periods of the internal waves in the lee of the sill are gradually reduced and the amplitudes of these waves are increased as the grid size is reduced from 100 m down to 12.5 m. With a further reduction in grid size, more short time and space scale motions become superimposed on the internal waves. Associated with the internal wave activity there is a deeper separation point that is fairly robust to all parameters investigated. Another separation point nearer to the top of the sill appear in the numerical results from the high resolution studies with the non-hydrostatic model. Associated with this shallower separation point, an overturning vortex appear in the same set of numerical solutions. This vortex grows in strength with reduced grid size in the non-hydrostatic experiments. The effects of the non-hydrostatic pressure on the velocity and temperature fields grow with reduced grid size. In the experiments with horizontal grid sizes equal to 100 m or 50 m the non-hydrostatic pressure effects are small. For smaller grid sizes also the time mean velocity and temperature fields are clearly affected by the non-hydrostatic pressure adjustments.

Keywords Non-hydrostatic · ocean modelling · tides · sills · internal waves · grid resolution

1 Introduction

Numerical ocean models are now widely used both in basic science studies, in studies of the climate, in engineering, and in the management of marine resources, see Haidvogel and Beckmann (1999); Kantha and Clayson (2000); Griffies (2004). Most simulations are presently done with hydrostatic models. The hydrostatic assumption simplifies the numerical computations considerably, and has facilitated numerous interesting studies of oceanic flow. However, as the horizontal resolution of the ocean models is gradually refined with increasing computer power, the validity of the hydrostatic assumption may, depending both on the problems addressed and the grid sizes used, become questionable. Non-hydrostatic ocean models are therefore used in many recent studies, see for instance Marshall et al. (1997b,a); Cummins et al. (2003); Legg and Adcroft (2003); Kanarska and Maderich (2003); Berntsen and Furnes (2005); Berntsen et al. (2006); Hodges et al. (2006); Kanarska et al. (2007); Lamb (2007); Xing and Davies (2007).

Since non-hydrostatic models are more complicated and time consuming to use, it will be important to establish some guidelines for when it is necessary to include the non-hydrostatic pressure effects. Scale analysis may be used to determine such criteria. In Marshall et al. (1997b) the non-hydrostatic parameter $n = \gamma^2/R_i$ is suggested. In this expression R_i is the Richardson number, γ is the aspect ratio h/L, and h and L are characteristic vertical and horizontal length scales, respectively. If $n \ll 1$, the motion is hydrostatic. If the stratification is weak, and processes on small horizontal length scales are important, this criterion may not be satisfied, and the use of non-hydrostatic models should be considered. However, to model the non-hydrostatic processes, the grid size must also be chosen small enough to facilitate a good representation of the phenomena that are influenced by the non-hydrostatic pressure effects. Therefore, when considering to apply a non-hydrostatic model, both the relevant parameters and length scales of the problem and the grid sizes one may afford to apply should be taken into account.

One may also consider to compute non-hydrostatic screening parameters to locate areas where non-hydrostatic pressure effects may be important. The non-hydrostatic screening parameter may be used to decide during run-time where and when the non-hydrostatic pressure and corresponding velocity corrections should be computed. Preliminary results based on this approach are presented in Wadzuk and Hodges (2004).

A third approach will be to consider more specifically important physical processes where non-hydrostatic pressures are expected to be significant. Focusing on such processes one may run a numerical model both with and without non-hydrostatic pressure effects for a range of grid sizes, thus allowing processes on gradually smaller scales to play a role as the grid size is reduced. Using this approach, we may obtain better qualitative and quantitative information about the non-hydrostatic pressure effects than what may be obtained through for instance scale analysis. This approach is used in the present study, and the focus is on tidally driven flow over a sill in a stratified fjord or loch. Fjords may be regarded as laboratories to investigate baroclinic processes, and in particular processes near sills where energy is transferred by non-linear effects from large to small scales and eventually mixing, see for instance Stigebrandt (1976); Stigebrandt and Aure (1989); Stigebrandt (1999); Farmer and Freeland (1983); Farmer and Armi (1999); Cummins et al. (2003); Stacey and Gratton (2001); Klymak and Gregg (2001, 2003, 2004); Inall et al. (2004, 2005); Vlasenko et al. (2002).

The tidally driven processes near Knight Inlet, British Columbia, have in particular been well investigated using both measurements (Farmer and Armi (1999); Armi and Farmer (2002); Klymak and Gregg (2001, 2003, 2004)), and numerical model experiments (Stacey (1985); Cummins (2000); Afanasyev and Peltier (2001a); Klymak and Gregg (2003); Cummins et al. (2003); Lamb (2004). Hydrostatic, non-hydrostatic, rigid-lid, and free surface models are used, and the studies are performed with both slip and no-slip bottom boundary conditions. A wide range of grid sizes, horizontally and vertically, and subgrid scale closure schemes is applied in these studies. The sensitivity of the flow to the stratification is also investigated. To facilitate high resolution numerical studies, two-dimensional (2D) versions of the numerical models are typically used with grid sizes in the range from approximately 1 to 200 m. Important three-dimensional (3D) effects (Klymak and Gregg (2001, 2004)) that also may play an important role in the creation of the downstream wedge discussed in several recent papers (Afanasyev and Peltier (2001a); Farmer and Armi (2001); Afanasyev and Peltier (2001b)), are neglected in the 2D studies. To facilitate 3D studies, coarser grids than those used in the 2D studies may have to be used. In the process of setting up the 3D model, appropriate grid sizes and turbulence closures have to be chosen, and the decision on whether to include non-hydrostatic pressure has to be made. Possible consequences of too coarse grid sizes and of neglecting the non-hydrostatic pressure effects should be considered.

Tidally driven processes have also recently been investigated in Loch Etive, see Inall et al. (2004, 2005). Motivated by the Loch Etive measurements Xing and Davies (2006a,b), hereafter XD06a and XD06b, and Davies and Xing (2007) applied idealised cross sectional models of Loch Etive to get further insight into how barotropic tidal energy is converted into internal waves and mixing. The sill depth at Loch Etive is approximately 15 m, whereas the corresponding depth at Knight Inlet is approximately 60 m. The processes and energy transfers near the sill are affected by the sill depth, and Loch Etive may therefore be regarded as a suitable study area for fjords or lochs with sills that are shallower than the sill in Knight Inlet. The supercritical stratified tidal flow in Loch Etive is also recently analysed in Stashchuk et al. (2007) using a non-hydrostatic model. The importance of non-hydrostatic pressure effects for this system is demonstrated in Xing and Davies (2007).

For tidally forced flow over sills the transfer of energy from the scale of the incoming tide towards the scales associated with internal waves, horizontal small scale eddies, overturning rolls, and eventually irreversible mixing may be very strong, see for instance Inall et al. (2004); Klymak and Gregg (2004). The long range of spatial and temporal scales involved and the strong non-linearities make numerical modelling of these systems very challenging. With present computer resources it is not feasible to resolve all relevant scales and one must keep in mind that the numerical results will be sensitive both to the grid size and to the choice of subgrid scale closure.

In the numerical experiments reported in Xing and Davies (2007), the vertical grid size was 1 m and the horizontal grid size varied gradually from 10 m in the sill region to 100 m outside this area. These model simulations were performed with with the MITgcm, see Marshall et al. (1997b,a); Adcroft et al. (1999). In Berntsen et al. (2008) the sensitivity of the numerical results for the idealised Loch Etive to the grid resolution was investigated using equidistant grid sizes ranging from 100 m to 12.5 m. These studies were performed with a cross sectional non-hydrostatic σ-coordinate model, see Berntsen et al. (2006). Detailed observations of tidally driven flow near sills reveal small scale process (Farmer and Armi (1999)), and we may expect strong non-hydrostatic pressure gradients associated with internal waves and instabilities in such systems. One may therefore ask whether the grid sizes used in Xing and Davies (2007) were sufficient to capture the full strength of the non-hydrostatic pressure effects. In Stashchuk et al. (2007) for instance the horizontal grid size used was 2.5 m.

The choice of problem for investigation of non-hydrostatic effects may also be based on analysis of the rate of change of the vertical velocity $\frac{Dw}{Dt}$ where w is the vertical velocity and $\frac{D}{Dt}$ the material derivative. For strong flow over a sill that is short and steep, like the one in Loch Etive, one may expect large values of $\frac{Dw}{Dt}$ near the sill and therefore strong non-hydrostatic effects. However, in a numerical model, the computed values of w may be regarded as average values of vertical velocity over the grid cells. The computed values of w and $\frac{Dw}{Dt}$ will therefore tend to decrease in magnitude with coarser grid sizes. For the same reason one may expect that the differences between the results from hydrostatic and non-hydrostatic numerical studies of flow over a sill are reduced if the grid size is increased.

The strength of the non-hydrostatic effects depends on $\frac{Dw}{Dt}$, which in a numerical model is forced via the gradients of the non-hydrostatic pressure by the local divergence or convergence in the model cells. The divergence/convergence is in each model cell computed from provisional 'hydrostatic' velocities, see Kanarska and Maderich (2003); Berntsen and Furnes (2005); Kanarska et al. (2007). Both $\frac{Dw}{Dt}$ and the divergence/convergence are strongly affected by the viscosity and diffusivity. To explore some of this sensitivity, the numerical experiments to be described are performed with two sets of values for viscosity and diffusivity.

In the present study we follow up previous studies of flow over a sill. The model domain is focused more around the sill and thereby studies with equidistant horizontal grid sizes in the range from 100 m down to 1.5625 m are facilitated. The sensitivity of the non-hydrostatic pressure effects to the grid size is investigated, and possible non-hydrostatic effects on the time mean flow are also studied. The model applied is a non-hydrostatic cross sectional σ-coordinate model, see Berntsen et al. (2006).

The numerical ocean modelling community is moving towards higher resolution, non-hydrostatic models, and the viscosities and diffusivities are often reduced with the grid size. The primary objective of this study is to examine in a region of significant non-hydrostatic effects, the sensitivity of the computed solutions to the grid size and to the non-hydrostatic pressure effects. Although previous studies of flow in sill regions have been performed, systematic convergence studies as suggested here have to the authors knowledge not been undertaken. The insight gained will be particularly important as calculations move to 3D where computational limitations will restrict the grid size to relatively coarse grids.

In Section 2 the numerical experiments are described. A detailed discussion of the results is given in Section 3. A summary and a general discussion are given in Section 4.

2 The numerical experiments

The σ-coordinate ocean model applied in the present studies is a two dimensional, (x, z), version of the model described in Berntsen (2000) where x and z are the horizontal and vertical Cartesian coordinates respectively. The model is available from www.math.uib.no/BOM/. The variables are discretized on a C-grid. In the vertical, the standard σ-transformation, $\sigma = \frac{z-\eta}{H+\eta}$, where η is the surface elevation, and H the bottom depth, is applied. For advection of momentum and density a Total Variance Diminishing (TVD)-scheme with a superbee limiter described in Yang and Przekwas (1992) is applied in the present studies. The standard second order Princeton Ocean Model (POM) method is applied to estimate the internal pressure gradients (Blumberg and Mellor (1987); Mellor (1996)). The model is mode split with a method similar to the splitting described in Berntsen et al. (1981) and Kowalik and Murty (1993). In the 2D model, all variations in the cross channel direction, y, are neglected, and all $\partial/\partial y$ terms in the governing equations are accordingly set to zero. There will still be cross channel velocities due to the Coriolis effect since the Coriolis frequency f is equal to 1.2×10^{-4} s^{-1}, a value typical of northern latitude regions.

In the model, the total pressure P is split into three components $P = P_\eta + P_{int} + P_{NH}$ where P_η is the pressure due to the free surface elevation, P_{int} is the internal pressure, and P_{NH} is the non-hydrostatic pressure. Using a splitting technique, the non-hydrostatic pressure P_{NH} may be computed by inserting the expressions for the non-hydrostatic velocity corrections into the equation of continuity (Kanarska and Maderich (2003); Heggelund et al. (2004)). Due to the σ-transformation, additional terms appear in the pressure equations, which complicates the computations. An alternative method, that has been adopted in the present study, is to view the non-hydrostatic pressure directly as $P_{NH}(x, \sigma, t)$, where t is time, or a pressure due to convergence or divergence in the σ-coordinate system (Berntsen and Furnes, 2005).

The time steps are performed with a predictor-corrector method where the leapfrog method is used as the predictor and the fully implicit method is used as the corrector.

The model has recently been applied to study lock release gravity currents and the propagation of solitary waves up an incline (Berntsen et al. (2006)) and the results are related to measurements from laboratory experiments and to corresponding results from the MITgcm (Marshall et al., 1997b,a; Adcroft et al., 1999). The results produced with the BOM are generally consistent with corresponding results from the MITgcm. However, by using a σ-coordinate model a better representation of the processes in the bottom boundary layer may be achieved. In Berntsen et al. (2006) more details about the estimation of the non-hydrostatic pressure are given. For convergence studies of the BOM see Avlesen et al. (2001); Berntsen et al. (2006).

The set up of the numerical experiments is similar to that described in XD06a and Berntsen et al. (2008). The topography and the initial temperature field, Θ, are given in Fig. 1.

A simple linear equation of state is used to convert temperature to density, see Xing and Davies (2001). The initial buoyancy frequency N is $0.01\,\mathrm{s}^{-1}$ in all experiments. For unforced systems and constant N, the propagation of internal waves may be studied with linear models, see Cushman-Roisin (1994); Kundu and Cohen (2008). However, in the present study with strong tidal forcing of the flow over a shallow sill, see below, there will be a strong nonlinear transfer of energy from long to short scales as demonstrated and explained in XD06b also with constant buoyancy frequency.

The depth profile $H(x)$ in meters is specified according to

$$H(x) = \begin{cases} -50 + \frac{35}{1+(x/500)**4} \ , \ x < 0 \\ -100 + \frac{85}{1+(x/500)**4} \ , \ x > 0 \end{cases} \tag{1}$$

assuming $x = 0\,\mathrm{m}$ at the top of the sill. The model domain extends from $x =$ -1000 m to $x = 2000\,\mathrm{m}$ and both lateral boundaries are open. For sensitivity of the results to the slope steepness see XD06b.

There is no flow through the sea bed. Initially the water elevation is zero, and there is no flow.

Tidal flow is forced into the model domain through the left open boundary. At this left boundary a 10 grid cell wide flow relaxation zone (Martinsen and Engedahl (1987)) is added to the computational domain. The depth is constant and equal to the depth at $x =$ -1000 m in this zone. In the left boundary zone all components of the velocity field, the water elevation, and the temperature field are updated in each time step according to

$$\phi \,=\, (1-\alpha)\phi_{int} + \alpha\phi_{ext}, \tag{2}$$

where ϕ_{int} contains the unrelaxed values computed by the model and ϕ_{ext} is a specified external value. The relaxation parameter α varies smoothly from 0 at $x =$ -1000 m to 1 in the leftmost boundary cell, see Martinsen and Engedahl (1987).

The M_2 tide is forced into the domain by specifying an external velocity in the x-direction $u_{ext-left}(t)$ as

$$u_{ext-left}(t) = u_0 \sin(\omega_{M2} t)\,, \forall\, z\,, \tag{3}$$

where $\omega_{M2} \,=\, 0.000140526\,\mathrm{rad}\ \ \mathrm{s}^{-1}$ and $u_0 \,=\, 0.3\,\mathrm{m\,s}^{-1}$ in all experiments. The tidal forcing and the idealized topography is appropriate for Loch Etive and based on recent measurements in the region (Inall et al. (2004)). The purpose of the present studies is not to reach steady state, but to investigate the non-hydrostatic effects for various horizontal grid sizes. The non-hydrostatic effects vary throughout a tidal cycle, but they are similar at corresponding times in consecutive tidal cycles. The focus in this study is on the non-hydrostatic effects during the period leading up to maximum flow over the sill, and the experiments reported here are run for 1/4 T where T is the M_2 tidal period. This means that there is inflow through the left open boundary zone and outflow through the right open boundary zone in the whole simulation period. At the left open boundary the external values of the velocity components in the y and z directions are zero, and the external values of the temperature are kept equal to the initial temperature profile. The external values for the water elevation $\eta_{ext-left}(t)$ are computed as lateral averages of the water elevations η close to the left boundary zone

$$\eta_{ext-left}(t) \;=\; \frac{1}{10\Delta x}\int_{-1000m}^{-1000m+10\Delta x} \eta(x,t)dx\,. \tag{4}$$

At the outflow right boundary, 20 grid cells with constant depth equal to the depth at $x = 2000\,\mathrm{m}$ are added to the computational domain. The first 10 cells are used as an averaging zone, and the rightmost 10 cells are used as a flow relaxation zone. In the averaging zone the external values for the velocity in the x-direction $u_{ext-right}$ are computed as lateral averages of the model velocities in the x-direction u according to

$$u_{ext-right}(z,t) \;=\; \frac{1}{10\Delta x}\int_{2000m}^{2000m+10\Delta x} u(x,z,t)dx\,. \tag{5}$$

In the right flow relaxation zone equation (2) is used to update the model velocities. In this zone the relaxation parameter α varies smoothly from 0 at $x = 2000\,\mathrm{m} + 10\Delta x$ to 1 in the rightmost boundary cell. The use of equation (2) and this choice of $u_{ext-right}$ allows the average interior velocity profile to propagate smoothly through the open boundary. This averaging technique was first suggested in Berntsen et al. (2002) and is also used to compute external values of the velocity components in y and z directions, the water elevation, and the temperature field.

In the vertical 100 equidistant σ-layers are used in all experiments. Horizontally the grids applied are equidistant and the experiments are run with horizontal grid sizes Δx equal to 100 m, 50 m, 25 m, 12.5 m, 6.25 m, 3.125 m, and 1.5625 m in order to investigate how the non-hydrostatic effects are affected by the grid size. In the experiments with $\Delta x = 12.5\,\mathrm{m}$ the internal time step used is $0.56\,\mathrm{s}$, and 30 external time steps are used for each internal step. The time steps are scaled proportionally with Δx in the experiments with other grid resolutions in order to keep the Courant numbers equal in all experiments. One numerical experiment over 1/4 T with $\Delta x = 1.5625\,\mathrm{m}$ takes approximately 200 hours on the available computers and this constraint has made longer time integrations very difficult. To facilitate studies with this grid size, the length of the computational domain is also substantially reduced compared to the length of the domains used in XD06a,b; Davies and Xing (2007); Berntsen et al. (2008). With such a short domain, the quality of the results from numerical experiments extended over longer time will also be reduced due to false reflections at the open boundaries, see the discussion in XD06b. The detailed results from the present studies depend on the the initial flow field and the initial stratification. The internal wave field over the first quarter of the second tidal period will for instance differ from the corresponding field over the first tidal cycle, and we can not expect to achieve a periodic solution. However, by comparing the results at the time of maximum inflow from the first tidal cycle presented here with corresponding results from the second tidal cycle presented in XD06a; Davies and Xing (2007); Berntsen et al. (2008), we find that the wave patterns in the lee of the sill are very similar.

The experiments are performed with constant values of viscosity and diffusivity as in XD06a, that is: horizontal viscosity $A_h = 10^{-1}\,\mathrm{m}^2\,\mathrm{s}^{-1}$, vertical viscosity $A_V = 10^{-3}\,\mathrm{m}^2\,\mathrm{s}^{-1}$, horizontal diffusivity $K_h = 10^{-7}\,\mathrm{m}^2\,\mathrm{s}^{-1}$, and vertical diffusivity $K_V = 10^{-7}\,\mathrm{m}^2\,\mathrm{s}^{-1}$. These values of viscosities and diffusivities were maintained constant in one set of calculations. The values are small compared to the values typically used in ocean models with grid sizes of the order 1 km, and they are small enough to allow internal waves in the lee of the sill to be represented. With very small values of vertical and horizontal diffusivity, the mixing becomes primarily controlled by convective overturning and instabilities. However, due to the cascade of energy towards the grid scale in nonlinear systems, much larger values of the viscosities are needed, see XD06a,b; Berntsen et al. (2008). This set of values are in this paper referred to as ”small” values. In order to explore the sensitivity to the viscosity and diffusivity, the experiments are repeated with "large" values of viscosity and diffusivity namely: $A_h = 1\,\mathrm{m^2\,s^{-1}}$, $A_V = 10^{-2}\,\mathrm{m^2\,s^{-1}}$, $K_h = 10^{-3}\,\mathrm{m^2\,s^{-1}}$, and $K_V = 10^{-4}\,\mathrm{m^2\,s^{-1}}$. The sensitivity of the numerical results to the subgrid scale closure for this tidally driven system was also investigated in more detail in Berntsen et al. (2008).

The choices of viscosities and diffusivities given above are to some extent arbitrary even if there are some general guidelines. For instance, the first set of values are large enough to filter out the grid scale noise and at the same time small enough to allow the representation of the small scale physical processes in the lee of the sill. In studies like this, unique optimal values of the viscosities and the diffusivities may not be obtained. The values of these parameters used in comparable studies may differ by orders of magnitudes. The differences between the two corresponding sets of results produced with the small and the large values may therefore provide some insight in the uncertainties due to the choice of subgrid scale closure scheme.

To identify the sensitivity of the solution and the non-hydrostatic effects to the grid size, the experiments, with both sets of values of viscosity and diffusivity, are repeated using the hydrostatic assumption for all values of Δx.

In the experiments, the bottom stress vector $\boldsymbol{\tau}_{\mathbf{b}}(x,t)$ is specified by

$$\boldsymbol{\tau}_{\mathbf{b}}(x,t) = \rho_0 C_D \sqrt{u_b^2 + v_b^2}\,\mathbf{u}_{\mathbf{b}}(x,t) \tag{6}$$

where ρ_0 is the reference density, and u_b and v_b are the velocity components in the x-direction and the cross channel direction respectively. The drag coefficient C_D is given by

$$C_D = \max[0.0025, \frac{\kappa^2}{(ln(z_b/z_0))^2}] \tag{7}$$

and z_b is the distance of the nearest grid point to the bottom. The von Karman constant κ is 0.4 and the bottom roughness parameter is chosen to be $z_0 = 0.01m$, see Blumberg and Mellor (1987).

The following norm is used to measure the differences between model fields ϕ_H produced with the hydrostatic model and model fields ϕ_{NH} produced with the non-hydrostatic model

$$\parallel \phi_H - \phi_{NH} \parallel = \sqrt{\frac{1}{Area} \int_{0m}^{2000m} \int_{H(x)}^{\eta(x,t)} (\phi_H - \phi_{NH})^2 dx dz}\,, \tag{8}$$

where $Area$ is the area of the integration domain.

The differences between instantaneous fields produced with different methods may be large due to small shifts in the phase of the internal waves that occur in the lee of the sill during super-critical inflow. Therefore, also the time mean fields

$$(\overline{u}, \overline{w}, \overline{\Theta}) = \frac{1}{T/8} \int_{T/8}^{T/4} (u, w, \Theta) dt\,, \tag{9}$$

are computed to investigate whether the changes also affect these more robust means.

Errors in the internal pressure gradient estimation may be a problem in σ-coordinate models, see for instance Haney (1991); Mellor et al. (1998). However, in the present experiments with relatively small grid sizes these errors are small. For instance in experiments with $\Delta x = 100\,\mathrm{m}$ where the flow is driven only by the artificial internal pressure gradients, the absolute value of the velocity components remains smaller than $1 \times 10^{-5}\,\mathrm{m\,s^{-1}}$, see also Berntsen et al. (2008).

3 Results

The results from the calculations show that the maximum tidal velocity u across the sill is larger than $0.80\,\mathrm{m\,s^{-1}}$ in all calculations. Using the same definition of the densimetric Froude number Fr as in XD06a, that is $Fr = \frac{u}{NH_s}$ where H_s is the sill depth, we find that $Fr \sim 5.3$ at maximum inflow, see also the discussion in Farmer and Armi (1999) on the definition of the Froude number.

In Figs. 2 to 8 the instantaneous non-hydrostatic pressure fields P_{NH} at maximum inflow, $t = 1/4T$, for the experiments with small values of viscosities and diffusivities are given for all grid sizes. In order to demonstrate the effects of the non-hydrostatic pressure corrections on the primary model fields, the corresponding temperature fields at maximum inflow for both the non-hydrostatic and the hydrostatic experiments are also given for identical parameters. The amplitudes of the non-hydrostatic pressure oscillations increase as Δx is reduced down to $\Delta x = 3.125\,\mathrm{m}$. Notice that the contour interval (CI) is increased with reduced values of Δx down to this grid size. The length scales of these pressure oscillations are reduced with decreasing values of the grid size down to at least $\Delta x = 6.25\,\mathrm{m}$. The flow is forced by the gradients in the pressure. Therefore, for the problem considered here we may expect gradually stronger non-hydrostatic pressure effects on the primary variables (velocities, temperature, and density) as the grid size is reduced from 100 m down to approximately 3.125 m in the studies with small values of viscosities and diffusivities. Comparisons of the temperature fields after 1/4 T produced with and without the non-hydrostatic corrections of the velocity fields also support this conclusion. With $\Delta x = 100\,\mathrm{m}$, the temperature fields from the hydrostatic and the non-hydrostatic experiments are very similar. This suggests that with a coarse grid processes on short wavelengths are smoothed out, the horizontal convergence/divergence is reduced, and w and $\frac{Dw}{Dt}$ are reduced. As the grid size is reduced, the non-hydrostatic effects on the temperature field become gradually more apparent. With a hydrostatic model dispersion due to non-hydrostatic effects is not included, and one may experience non-linear steepening of fronts and internal waves. Associated with this, there is a stronger transfer of energy towards the shortest possible length scale $2\Delta x$ in a hydrostatic model. In Fig. 5c for $\Delta x =$

12.5 m we notice this steepening of the waves in the lee of the sill, and this tendency becomes more apparent as the grid size is further refined, see Figs. 6c to 8c.

In the lee of sills, one may in observations find bodies of well mixed fluid, see for instance the discussions of the processes generating the downstream wedge in Knight Inlet in Afanasyev and Peltier (2001a); Farmer and Armi (2001); Afanasyev and Peltier (2001b). The present studies indicate that with a hydrostatic model and sufficient spatial resolution, there may be a stronger transfer of energy towards the $2\Delta x$ scale, and then to irreversible mixing, that gradually builds up the body of well mixed fluid downstream. With a non-hydrostatic model, more of the energy remains in the internal wave field generated in the lee during super-critical inflow. With small enough grid sizes, overturning vortices that create mixing may be found in the numerical results produced by a non-hydrostatic model, see Figs. 7b and 8b. Thus, both types of models may create bodies of well mixed fluid in the lee. However, the mechanism when using a hydrostatic model is artificial, and hence it may be dubious to apply such a model in more quantitative studies of mixing.

In all experiments bottom boundary layer separation occurs in the lee of the sill approximately between 40 m to 65 m depth between 400 m and 550 m from the top of the sill, see Figs. 2 to 8. This agrees very well with the position of the measured separation point in Loch Etive reported in Inall et al. (2004), see their Fig. 5. The numerical separation point is fairly robust to the parameters investigated. A horizontal length scale of the horizontal movements of the separation point may be estimated from $\lambda = \frac{L_{sep}}{H_{sep}}\frac{U}{N}$, see Afanasyev and Peltier (2001a). Here L_{sep} is the horizontal extent of the region of the slope on the lee side where the separation occur (150 m), H_{sep} is the corresponding vertical extent (32 m), and U is a typical current speed near the separation point ($0.20\,\mathrm{m\,s^{-1}}$) giving a length scale λ of approximately 125 m consistent with the range found in our numerical studies.

In the results from all simulations, internal waves are found in the lee of the sill during maximum inflow, see Figs. 2 to 8. The length scales of these waves depend on the grid size. The length scales and the general shape of the internal waves may also be clearly affected by the non-hydrostatic pressure effects, especially in the high resolution studies. In the results produced with $\Delta x = 100\,\mathrm{m}$, the length scale of the downstream waves is approximately 1000 m in both the hydrostatic and the non-hydrostatic model results. With higher horizontal resolution, smaller scale waves may be represented, and we notice that the length scale of the waves is gradually reduced from 1000 m to approximately 2-300 m as Δx is reduced to 12.5 m in the non-hydrostatic studies, see Figs. 2b to 5b. In the results produced with the non-hydrostatic model and a grid size smaller than 12.5 m, these internal waves with length scales from 200 m to 300 m are still found, even if also smaller scale oscillations become superimposed on these waves as the grid is further refined, see Figs. 6b to 8b. In the results produced with the hydrostatic model, we may notice a similar reduction of the length scale of the internal waves as the grid size is reduced to $\Delta x = 12.5\,\mathrm{m}$. However, this length scale is also further reduced in the hydrostatic studies with smaller grid sizes than 12.5 m. In the numerical results produced with the hydrostatic model and $\Delta x = 1.5625\,\mathrm{m}$, we may notice waves with length scales down to approximately 50 m, see Fig. 8c and the discussion above on missing non-hydrostatic dispersion and steepening of waves in hydrostatic models.

The periods and amplitudes of the internal waves in the lee of the sill are correspondingly affected by the grid size. This is clearly seen in the time series of the vertical velocities (Fig. 9) taken at a point downstream of the sill at $(x, z) = (500\,\mathrm{m}, -20\,\mathrm{m})$. For all grid sizes used here, internal waves are generated when the flow over the sill becomes super-critical, $Fr > 1$, approximately after $t = 1/8$ T (or 93 minutes). As the vertical oscillations become more sinusoidal, they grow in amplitude, and the period is reduced as the grid size is reduced from 100 m to 12.5 m, see Fig. 9a. For $\Delta x = 12.5\,\mathrm{m}$, the period is approximately 7 minutes. As the grid size is further reduced from 12.5 m to 6.25 m, the amplitudes of the vertical velocity oscillations continue to grow at this point. However, these amplitudes are approximately the same in the experiments with $\Delta x = 6.25\,\mathrm{m}$, 3.125 m, and 1.5625 m. By comparing the results for $\Delta x = 12.5\,\mathrm{m}$ in Fig. 9a with corresponding results for finer grid sizes in Fig. 9b, it is apparent that with smaller Δx short time scale changes are added to the sinusoidal signals produced with $\Delta x = 12.5\,\mathrm{m}$, even if the periods of approximately 7 minutes are still visible in the high resolution results. The vertical oscillations are strongly affected by the hydrostatic assumption, see Figs. 9b and 10. With a grid size of 1.5625 m, the periods of these oscillations at (x, z) = (500 m, -20 m) are reduced to approximately 3 minutes, consistent with the shorter length scale oscillations seen in Fig. 8c. By comparing Figs. 9b and 10 we also notice stronger vertical accelerations, $\frac{\partial W}{\partial t}$, and that the negative vertical velocity components are much larger in magnitude ($\sim 1.5\ \mathrm{ms}^{-1}$) than the corresponding positive velocity components in the results from the hydrostatic study. In the hydrostatic experiments, forces from the non-hydrostatic pressure gradients acting against the downward flow in the lee are lacking, and the downward flow may therefore become unrealistically large in the high resolution hydrostatic studies (Fig. 10). See also the comment in Hodges et al. (2006) that improved grid refinement in a hydrostatic model may lead to worse results. The maximum values of the vertical velocity components in the non-hydrostatic experiments are $\sim 0.65\ \mathrm{ms}^{-1}$. The horizontal velocity components in the lee of the sill are of the same order of magnitude (Berntsen et al. (2008)). In the non-hydrostatic experiments these values are consistent with rotary overturning rolls as described in Farmer and Armi (1999).

The focus has so far been on the non-hydrostatic pressure effects on the instantaneous velocity and temperature fields. For some applications, where the focus is on the residual flow, it may be more relevant to study whether the velocity corrections due to non-hydrostatic pressure also affect the time mean fields. In order to investigate this, time means of the velocity components and the temperature field are computed, see Equation (9). The means are taken over the last half of the simulation period. These time mean fields on the lee side of the sill are given in Figs. 11 and 12. These results are produced with Δx = 1.5625 m, small and constant values of viscosity and diffusivity, and both the hydrostatic and non-hydrostatic mean fields are given. The non-hydrostatic pressure corrections clearly affect the downstream time mean fields. We notice for instance from Fig. 11 that near the surface in the outflow area there is still water warmer than 13 ℃ in the results from the hydrostatic experiment. The corresponding 13 ℃ contour is missing in the outflow area in the time mean field produced with the non-hydrostatic model. The changes on the 12 ℃ contour by introducing non-hydrostatic pressure are also noticeable. These changes in the time mean temperature field may be due to changes in the mixing. However, the time mean velocity fields are also affected by the non-hydrostatic pressure corrections, see Fig. 12 and the discussion below, and therefore changes in the advection may also contribute to the changes in the time mean temperature field.

In the non-hydrostatic results, the tongue of high velocity water near the surface extends much further downstream from the sill than in the corresponding hydrostatic results, notice for instance the $40\,\mathrm{cm\,s^{-1}}$ isolines in Fig. 12a and 12b. Near the top of the sill, on the downstream side of it, there is also a back-flow of water towards the sill in the time mean field from the non-hydrostatic experiment. This back-flow is missing in the results from the corresponding hydrostatic experiment. Associated with the horizontal back-flow, there is an upward flow of water in the lee of the sill in the time mean velocity field from the non-hydrostatic experiment. The computed time mean velocity fields suggest that in the non-hydrostatic results there is a strong vortex in the lee of the sill in the period of super-critical flow. The non-hydrostatic pressure gradients in the lee near the top of the sill may explain the separation of the flow and the generation of a vortex in the non-hydrostatic simulations, see Fig. 8a and the zoom in of this pressure in Fig. 13. The build up of the pressure field seen in Fig. 13 may qualitatively be understood from the Bernoulli equation, see Kundu and Cohen (2008), which strictly speaking is for inviscid, steady, barotropic flows. In the lee below the sill depth, the speed is reduced which means build up of a counter pressure and possible flow separation. The flow separation will create higher speeds further up in the water column, explaining the negative pressure seen in Fig. 14. The vortex in the lee creates enhanced mixing explaining at least partly the non-hydrostatic effects on the time mean temperature field (Fig. 11).

The flow separation in the lee and the overturning roll near the top of the sill are also seen in the plot of the instantaneous temperature field from the non-hydrostatic experiment (Fig. 8b) and in some of the non-hydrostatic results produced with Δx larger than 1.5625 m, see Figs. 2b to 7b. However, the vortex gradually becomes weaker with a coarser grid, and for Δx equal to 100 m or 50 m this overturning becomes both displaced and much weaker, see Figs. 2b and 3b. Thus with a too coarse grid to resolve the vortex, the model tends to filter these motions out.

Overturning may also be seen in some of the results produced by the hydrostatic model. During overturning we are using the hydrostatic model outside its domain of validity. Even if this easily may create instabilities, models based on the hydrostatic primitive equations may still be able to produce instances of inverse stratification. However, the overturning events produced by the hydrostatic model in the present study are generally weaker and more distorted than the corresponding events produced by the non-hydrostatic model, compare Figs. 7b and 7c and Figs. 8b and 8c.

The plots of the time mean temperature fields (Fig. 11) suggest that the deeper separation point approximately 500 m from the top of the sill is less affected by the non-hydrostatic pressure effects.

The second order norm, see Equation 8, may be used to measure the non-hydrostatic effects for different values of Δx, see Figs. 14 and 15. The non-hydrostatic effects on the time mean fields are generally much smaller than the effects on the instantaneous fields. The instantaneous fields from the non-hydrostatic experiments may be out of phase with the corresponding fields from the hydrostatic experiments creating fairly large values of this discrepancy measure. These short time scale effects tend to be filtered out in the time mean fields. However, there are noticeable non-hydrostatic effects also on the time mean fields, especially in the results from the experiments with small and constant values of viscosity and diffusivity. The results indicate that the effects on the time mean fields may become stronger as the grid size is reduced.

The non-hydrostatic pressure is driven by the local convergence/divergence into or out of the grid cells of the provisional hydrostatic velocity field. This convergence/divergence is strongly affected by the choice of viscosities and diffusivities. With large values of viscosity and diffusivity, small scale variability in the flow and in the temperature field will be smoothed out. We may expect less small scale convergence/divergence, and smaller non-hydrostatic pressure effects. This view may also find support in the results given in Figs. 14 and 15. For the smaller values of Δx, the non-hydrostatic pressure effects are much larger in the experiments with small values of viscosity and diffusivity. In the numerical experiments with large values of viscosity, the non-hydrostatic effects on the horizontal velocity field are generally small and also relatively robust to changes in Δx. For this case, the viscosity is large enough to suppress small scale variability in the flow field, and a reduction in Δx will not change the computed flow fields significantly.

The numerical investigations of non-hydrostatic pressure effects reported in Xing and Davies (2007) were performed with $\Delta x = 10\,\mathrm{m}$ near the sill, and with small and constant values of viscosity and diffusivity. The results presented here are consistent with their findings. However, the results given in Figs. 14 and 15 suggest that a further reduction of Δx from $10\,\mathrm{m}$ would have revealed even stronger non-hydrostatic effects.

4 Discussion

In this study the sensitivity of the non-hydrostatic pressure effects to the grid size is explored for the case of tidally driven stratified flow over a shallow sill in a loch. The study is motivated by earlier studies of the processes in Loch Etive based on both measurements and numerical investigations, see Inall et al. (2004, 2005); XD06a,b; Davies and Xing (2007); Xing and Davies (2007); Stashchuk et al. (2007); Berntsen et al. (2008). The non-hydrostatic pressure effects depend on the viscosity and the diffusivity and this sensitivity is also addressed. The simulations are performed both with a hydrostatic and a non-hydrostatic version of a terrain following ocean model, and horizontal grid sizes in the range from 100 m to 1.5625 m are used.

The characteristics of the flow are gradually changed as the grid size is reduced. The length scale of the internal waves appearing in the lee of the sill is for instance gradually reduced and the vertical motions become more sinusoidal as the grid size is reduced from 100 m to 12.5 m. With a further reduction of the grid size, more short time scale signals are gradually superimposed on these sinusoidal internal waves. Associated with the internal waves in the lee, there is a flow separation point. The position of this point is very robust to the parameters explored, and agrees well with the position of the measured separation point in Loch Etive.

In many studies it may be more important to get the larger scale mean characteristics of the flow and the hydrography correct, than to capture all details of the flow. This study shows that there are strong non-hydrostatic effects both on the time mean flow field and the time mean density field. Consequently a model must have sufficient resolution to resolve the adjustments of the fields by the non-hydrostatic pressure.

In the numerical results produced with the non-hydrostatic model and an adequate grid size, we find flow separation also near the top of the sill in the lee, and an overturning vortex associated with the flow separation. This vortex is not found in the results from the non-hydrostatic model using grid sizes of

100 m or 50 m. This vortex is also found in the time mean fields from the non-hydrostatic experiments, but not in the corresponding fields produced with the hydrostatic model. By using the non-hydrostatic model and reducing the horizontal grid size from 25 m down to 3.125 m, the vortex gradually grows in strength. In the results produced with a grid size of 1.5625 m, the overturning roll is almost equal to the same roll produced with a grid size of 3.125 m. It would be tempting to conclude from this that the essential features of the vortex are resolved with a grid size of 3.125 m. However, this may rather indicate that for the finest grid size, the values of viscosity chosen are large enough to prohibit further modifications of the vortex. The experiments with even larger values of viscosity and diffusivity also show that the importance of the non-hydrostatic model pressure adjustments clearly depend on the degree of smoothing of the model fields, and for larger values of viscosity/diffusivity the non-hydrostatic effects may not continue to grow as the grid size is reduced.

In numerical ocean modelling there is a general trend towards higher resolution and non-hydrostatic models. Below we will try to put the present work in this wider perspective.

In large scale ocean modelling based on the Reynolds averaged equations (RANS) with grid sizes larger than ~ 1 km the hydrostatic approximation is valid, see Marshall et al. (1997b). Grid convergence may be demonstrated in RANS type simulations by using large values of eddy viscosity and eddy diffusivity. In Avlesen et al. (2001) for instance it was shown that the numerical results from the present model and the Princeton Ocean Model (POM), see Blumberg and Mellor (1987); Mellor (1996), converged to the same solution for density driven flow in a closed basin using large and constant values of viscosity and diffusivity.

At the other end of the spectrum are the DNS (Direct Numerical Simulations) models. Using DNS all relevant scales are resolved and parameterizations are not required. The grid size in DNS studies is $\sim$ 1 mm and therefore it is not feasible to apply DNS on ocean scale problems. However, it may still be a good approach to test the non-hydrostatic ocean models on laboratory scale problems, see Rickard et al. (2009). In Berntsen et al. (2006) it was also shown that the MITgcm (Marshall et al. (1997b,a)) and the present model produced grid converged solutions in lock release tank scale experiments.

A more tractable alternative is to apply Large Eddy Simulations (LES). This will require a grid size in all spatial directions of $\sim 1\,\mathrm{m}$. In general this will probably not be possible in numerical studies on ocean scale within the foreseeable future (Fringer, 2009). The idealised 2D experiments described here with $\sim 1.5\,\mathrm{m}$ resolution may, however, qualify as LES simulations.

In the near future it will be more realistic to apply grid sizes in the range between $\sim 1\,\mathrm{km}$ and $\sim 1\,\mathrm{m}$. In this range non-hydrostatic pressure effects may be important, even if they are not fully accounted for as in LES or DNS. The focus in this study has been on demonstrating that these non-hydrostatic effects may gradually become stronger as the grid size is reduced towards the grid scale associated with LES. When using small values of viscosity and diffusivity to allow smaller scale phenomena to appear with smaller grid size, grid convergence may have to be sacrificed. With larger values of eddy viscosity and eddy diffusivity or weaker tidal forcing, solutions that are robust to the grid size may be produced, see Berntsen et al. (2008). However, larger values of viscosity/diffusivity also means that real physical phenomena that could have been represented with the chosen grid size, may not appear in the numerical results.

The results from the present studies indicate that for larger grid sizes, $50\,\mathrm{m}$ or $100\,\mathrm{m}$ in our case with tidally driven flow over a sill, the non-hydrostatic pressure effects are relatively small. This finding has important consequences for the planning of future 3D experiments for such systems. Unless we can afford to apply a small enough horizontal grid size, it may be a waste of computer time to perform 3D sill studies with non-hydrostatic models.

In high resolution DNS studies, one may expect to find important 3D features of the flow superimposed on the 2D phenomena described here, see for instance Dörnbrack (1998); Carnevale et al. (2001); Fringer and Street (2003); Smyth et al. (2005). The volume of the model domains in DNS studies is, with the present computer systems, typically of the order $1\,\mathrm{m}^3$. Thus it will not be feasible today to perform DNS studies for a realistic sill domain. At present we therefore do not know how much more the numerical solutions will change if we continue to refine the grid. However, with a horizontal grid size of 1.5625 m we are at least able to represent both the internal waves and the overturning vortices in the lee of the sill. Both processes are strongly non-hydrostatic and important for the mixing in the lee of sills, see the very interesting discussions on the topic in Afanasyev and Peltier (2001a,b); Farmer and Armi (2001).

It will be natural to ask for a better validation of the model using both model results and measurements from the real sill area. Such a comparison requires high resolution measurements from the study area. In addition, detailed information about all forcing variables and all details of the topography including stones and possible seaweed are needed to force the model and to ensure accurate descriptions of the depth and the bed stress. Stones, gravel, and seaweed may even interact with the flow and complicate a clean comparison between measurements and model results. For the present 2D study, the lack of all cross channel variability further complicates a quantitative validation procedure based on measurements.

There is a growing literature pointing at the importance of the interactions between stratified flow and topography and the associated irreversible mixing on the meridional overturning circulation, see for instance Wunsch (1970); Polzin et al. (1997); Samelson (1998); Munk and Wunsch (1998); Spall (2001); Fringer and Street (2003); Kunze and Llewellyn Smith (2004); Wunsch and Ferrari (2004). The grid resolution of large scale models will in the foreseeable future be far to coarse to allow a good representations of these interactions and the mixing. Consequently the quality of the model outputs from the large scale ocean models rely heavily on the quality of the parameterizations of the subgrid scale (SGS) processes that they use. The remark made in Griffies (2004): " there remains a large degree of uncertainty in the SGS schemes appropriate for ocean climate simulations" is unfortunately still valid. A possible way forward may be to produce model results that capture the essential features of the interactions between stratified flow and topography and the associated irreversible mixing, using high resolution, non-hydrostatic, preferably 3D, ocean models. Time mean fields of the primary variables may be derived from the high resolution model fields. The exercises may be repeated with hydrostatic coarse resolution models to investigate whether the models in combination with the chosen parameterizations are able to reproduce the mean fields from the high resolution studies. Fjord or Loch areas may be very suitable for such exercises, and possible mismatches may also hopefully lead to improvements of the parameterizations.

Acknowledgements. This work was done during the first author's sabbatical year at Proudman Oceanographic Laboratory. He thanks the people at the laboratory for their great hospitality, and the Faculty of Mathematics and Natural Sciences, University of Bergen, for support during the sabbatical year. The authors also thank two reviewers for valuable remarks.

Figure captions

Fig. 1. Topography and initial temperature field.

Fig. 2. The non-hydrostatic pressure field P_{NH} (top figure) after 1/4 T for $\varDelta x = 100.0\,\mathrm{m}$ for the non-hydrostatic experiment with small values of viscosity and diffusivity. Negative pressures are indicated with dashed lines. The temperature field after 1/4 T for the same experiment is given in the middle figure. The corresponding temperature field for the hydrostatic experiment is given in the bottom figure.

Fig. 3. As Fig. 2, except $\varDelta x = 50.0\,\mathrm{m}$.

Fig. 4. As Fig. 2, except $\varDelta x = 25.0\,\mathrm{m}$.

Fig. 5. As Fig. 2, except $\varDelta x = 12.5\,\mathrm{m}$.

Fig. 6. As Fig. 2, except $\varDelta x = 6.25\,\mathrm{m}$.

Fig. 7. As Fig. 2, except $\varDelta x = 3.125\,\mathrm{m}$.

Fig. 8. As Fig. 2, except $\varDelta x = 1.5625\,\mathrm{m}$.

Fig. 9. Time series of vertical velocities at $(x, z) = (500\,\mathrm{m}, \text{-}20\,\mathrm{m})$. The time is given in minutes. The results are for the non-hydrostatic experiments with small values of viscosity and diffusivity. In the top figure the values for $\varDelta x = 100\,\mathrm{m}$ (solid line-small amplitudes), $\varDelta x = 50\,\mathrm{m}$ (dotted line), $\varDelta x = 25\,\mathrm{m}$ (dashed line), and $\varDelta x = 12.5\,\mathrm{m}$ (solid line-large amplitudes) are given. In the bottom figure the values for $\varDelta x = 6.25\,\mathrm{m}$ (dotted line), $\varDelta x = 3.125\,\mathrm{m}$ (dashed line), and $\varDelta x = 1.5625\,\mathrm{m}$ (solid line) are given for the last part of the simulation period.

Fig. 10. Time series of vertical velocities at $(x, z) = (500\,\mathrm{m}, \text{-}20\,\mathrm{m})$. The time is given in minutes. The results are for the hydrostatic experiment with small values of viscosity and diffusivity and $\varDelta x = 1.5625\,\mathrm{m}$.

Fig. 11. The time mean temperature field for the non-hydrostatic experiment with small values of viscosity and diffusivity and $\Delta x = 1.5625\,\mathrm{m}$ (top figure), and the corresponding temperature field for the hydrostatic experiment in the bottom figure. The time means are taken for the period from 1/8 T to 1/4 T.

Fig. 12. The time mean horizontal velocity field for the non-hydrostatic experiment with small values of viscosity and diffusivity and $\Delta x = 1.5625\,\mathrm{m}$ (top figure), and the corresponding velocity field for the hydrostatic experiment in the bottom figure.

Fig. 13. The non-hydrostatic pressure field P_{NH} in the lee of the sill near the top for $\Delta x = 1.5625\,\mathrm{m}$ for the non-hydrostatic experiment with small values of viscosity and diffusivity. Negative pressures are indicated with dashed lines. The field after 1/4 T is given in a) and the time mean non-hydrostatic pressure field is given in b).

Fig. 14. The norms of the differences between the instantaneous temperature fields after 1/4 T produced with the non-hydrostatic model and the corresponding field produced with the hydrostatic model, see Equation 8, are given in the top figure as functions of Δx. The results for the experiments with large values of viscosity and diffusivity are given with circles and the results for the experiments with small values of viscosity and diffusivity are given with squares. The norms of the corresponding differences between the time mean temperature fields, see Equation 9, are given in the bottom figure.

Fig. 15. The norms of the differences between the instantaneous horizontal velocity fields after 1/4 T produced with the non-hydrostatic model and the corresponding field produced with the hydrostatic model, see Equation 8, are given in the top figure as functions of Δx. The results for the experiments with large values of viscosity and diffusivity are given with circles and the results for the experiments with small values of viscosity and diffusivity are given with squares. The norms of the corresponding differences between the time mean horizontal velocity fields, see Equation 9, are given in the bottom figure.

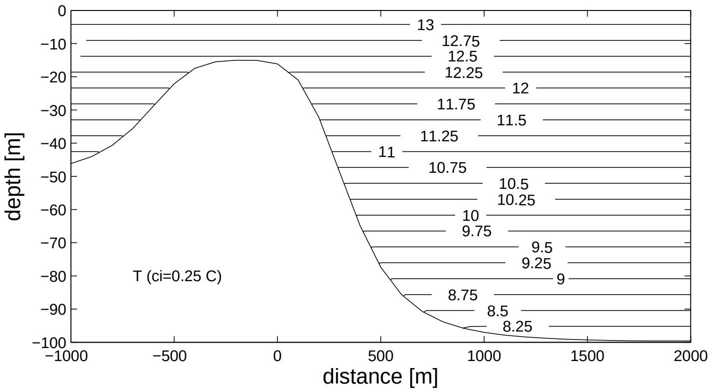

Fig. 1 Topography and initial temperature field.

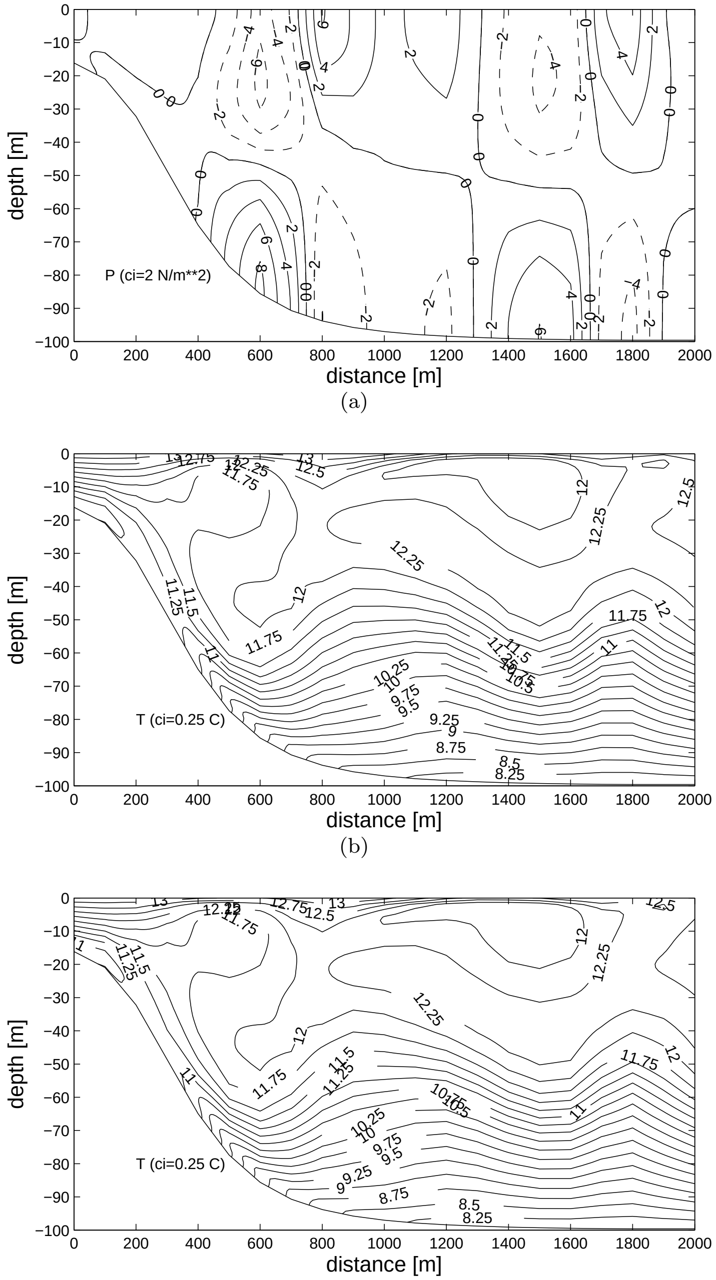

(a) (b) (c)

Fig. 2 The non-hydrostatic pressure field P_{NH} (top figure) after 1/4 T for $\Delta x = 100.0$ m for the non-hydrostatic experiment with small values of viscosity and diffusivity. Negative pressures are indicated with dashed lines. The temperature field after 1/4 T for the same experiment is given in the middle figure. The corresponding temperature field for the hydrostatic experiment is given in the bottom figure.

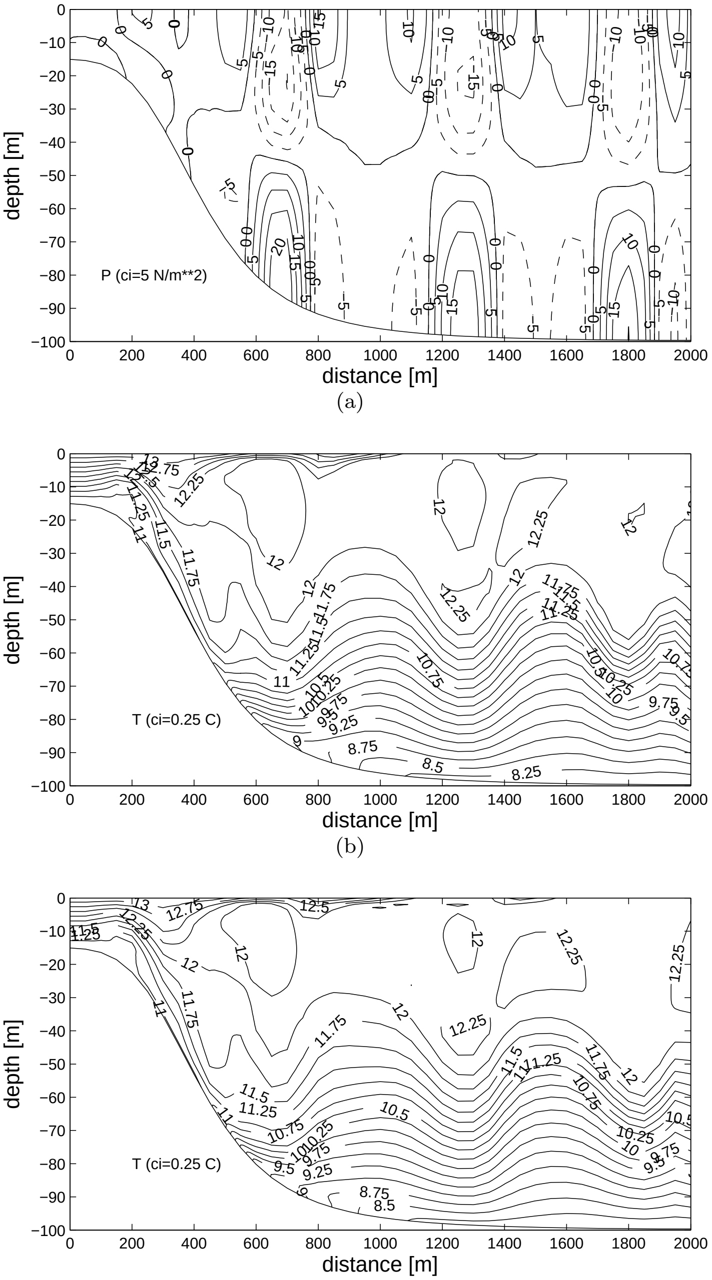

(a)

(b)

(c)

Fig. 3 As Fig. 2, except $\Delta x = 50.0\,\text{m}$.

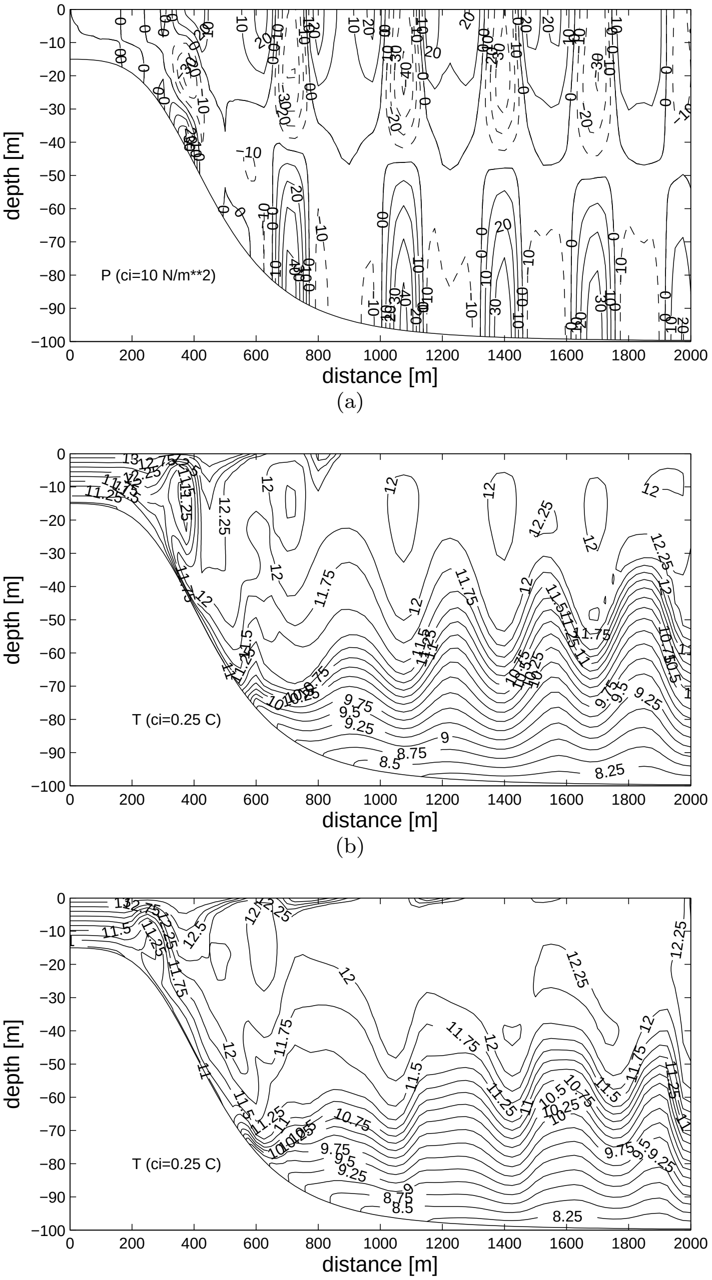

(a)

(b)

(c)

Fig. 4 As Fig. 2, except $\Delta x = 25.0\,\mathrm{m}$.

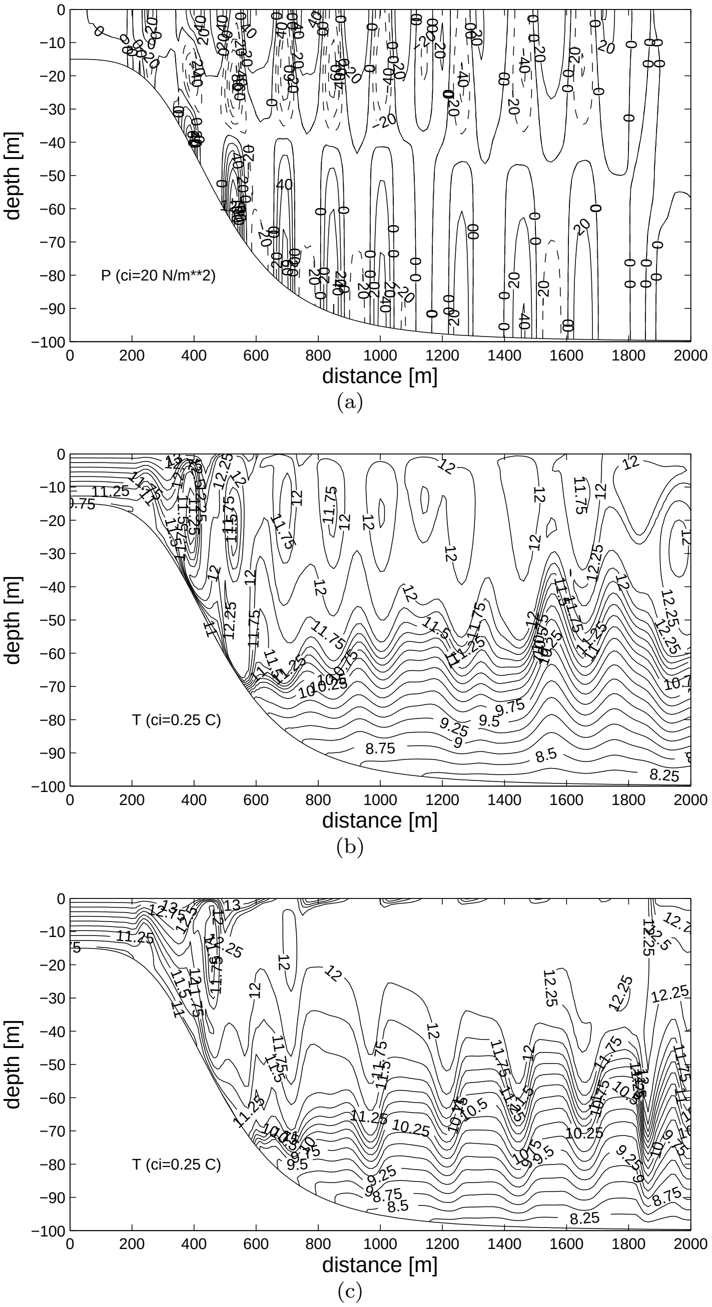

Fig. 5 As Fig. 2, except $\Delta x = 12.5\,\mathrm{m}$.

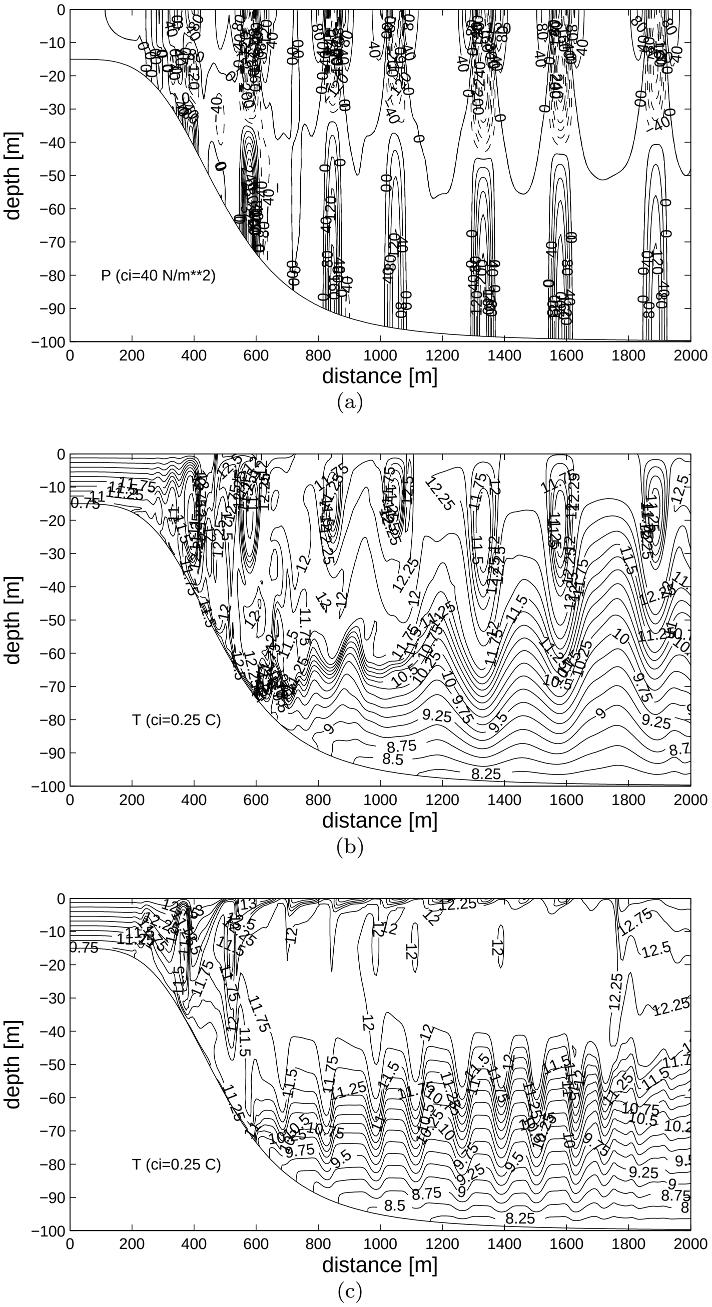

Fig. 6 As Fig. 2, except $\varDelta x = 6.25\,\mathrm{m}$.

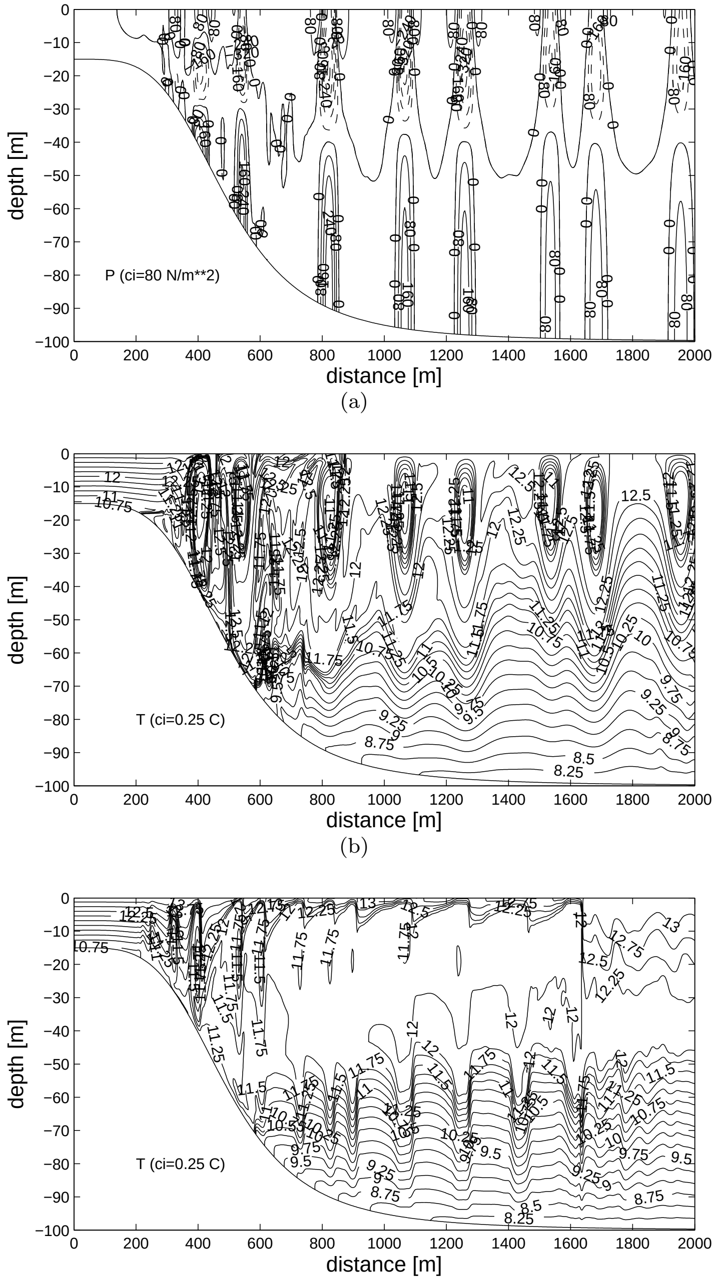

(a)

(b)

(c)

Fig. 7 As Fig. 2, except $\Delta x = 3.125\,\mathrm{m}$.

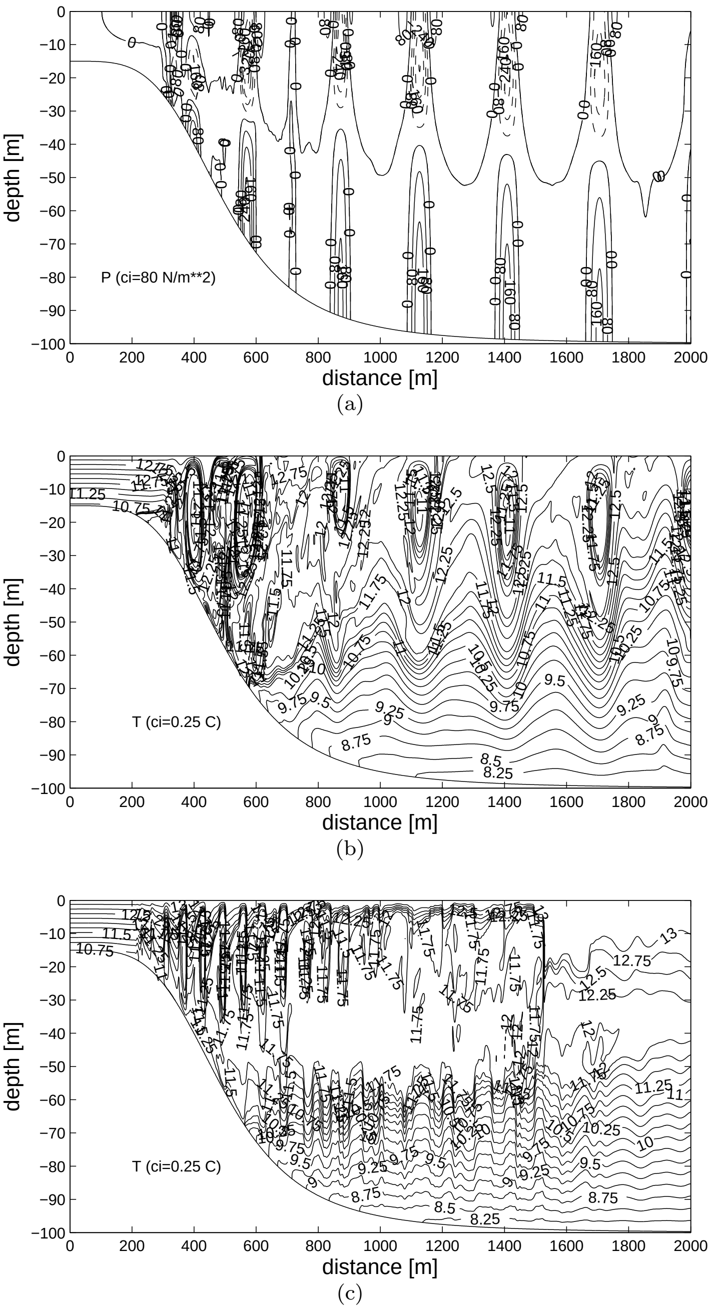

Fig. 8 As Fig. 2, except $\Delta x = 1.5625\,\mathrm{m}$.

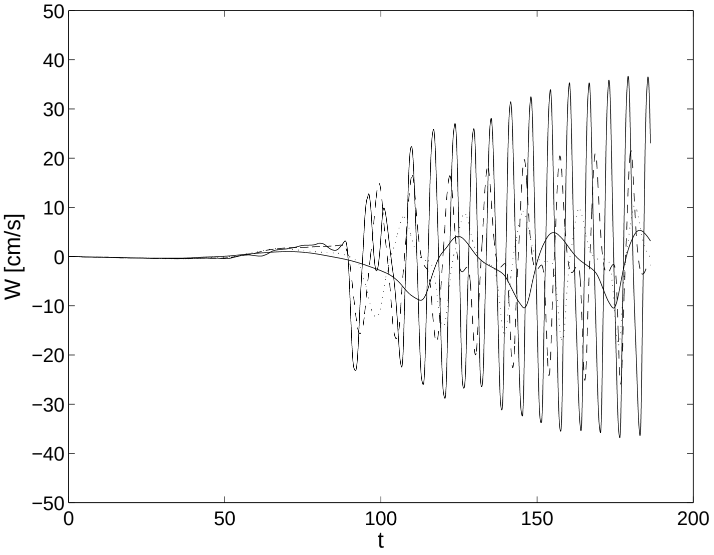

(a)

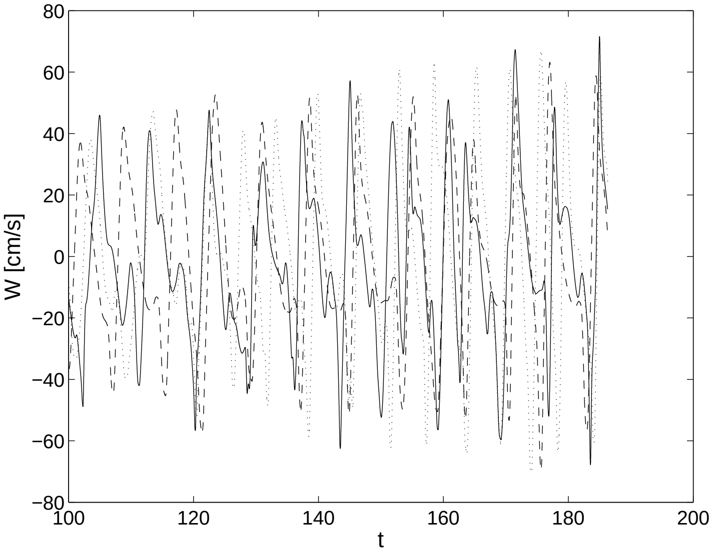

(b)

Fig. 9 Time series of vertical velocities at (x, z) = (500 m, -20 m). The time is given in minutes. The results are for the non-hydrostatic experiments with small values of viscosity and diffusivity. In the top figure the values for $\Delta x = 100\,\mathrm{m}$ (solid line-small amplitudes), $\Delta x = 50\,\mathrm{m}$ (dotted line), $\Delta x = 25\,\mathrm{m}$ (dashed line), and $\Delta x = 12.5\,\mathrm{m}$ (solid line-large amplitudes) are given. In the bottom figure the values for $\Delta x = 6.25\,\mathrm{m}$ (dotted line), $\Delta x = 3.125\,\mathrm{m}$ (dashed line), and $\Delta x = 1.5625\,\mathrm{m}$ (solid line) are given for the last part of the simulation period.

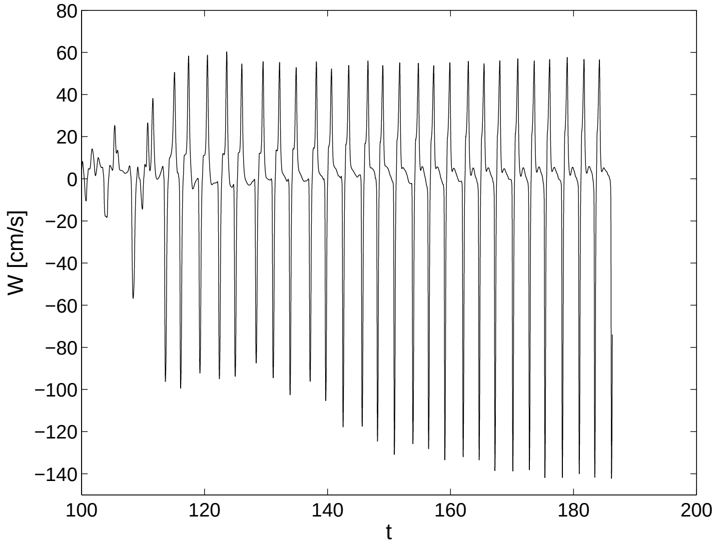

(a)

Fig. 10 Time series of vertical velocities at (x, z) = (500 m, -20 m). The time is given in minutes. The results are for the hydrostatic experiment with small values of viscosity and diffusivity and $\Delta x = 1.5625\,\mathrm{m}$.

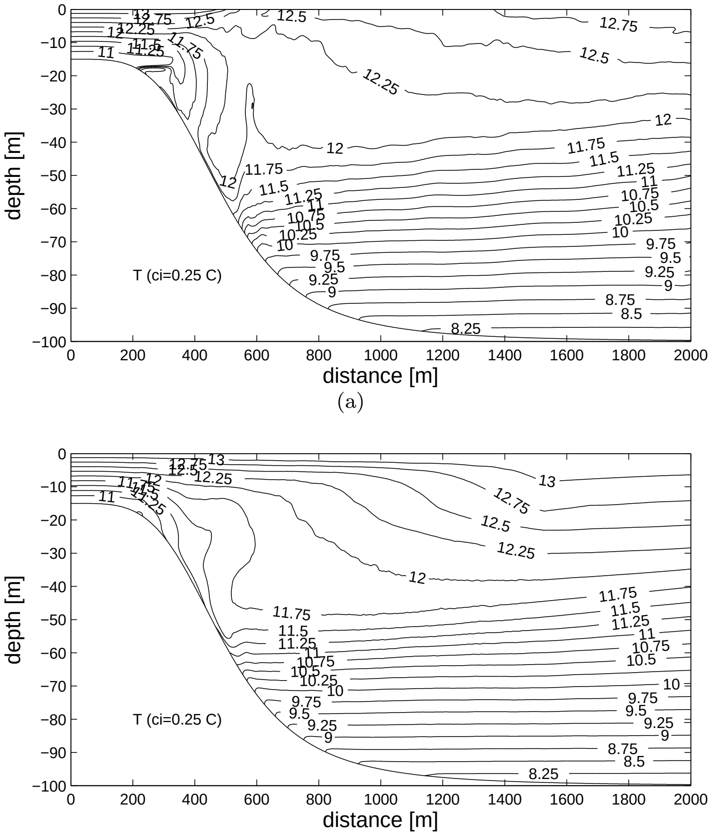

(a)

(b)

Fig. 11 The time mean temperature field for the non-hydrostatic experiment with small values of viscosity and diffusivity and $\Delta x = 1.5625\,\mathrm{m}$ (top figure), and the corresponding temperature field for the hydrostatic experiment in the bottom figure. The time means are taken for the period from 1/8 T to 1/4 T.

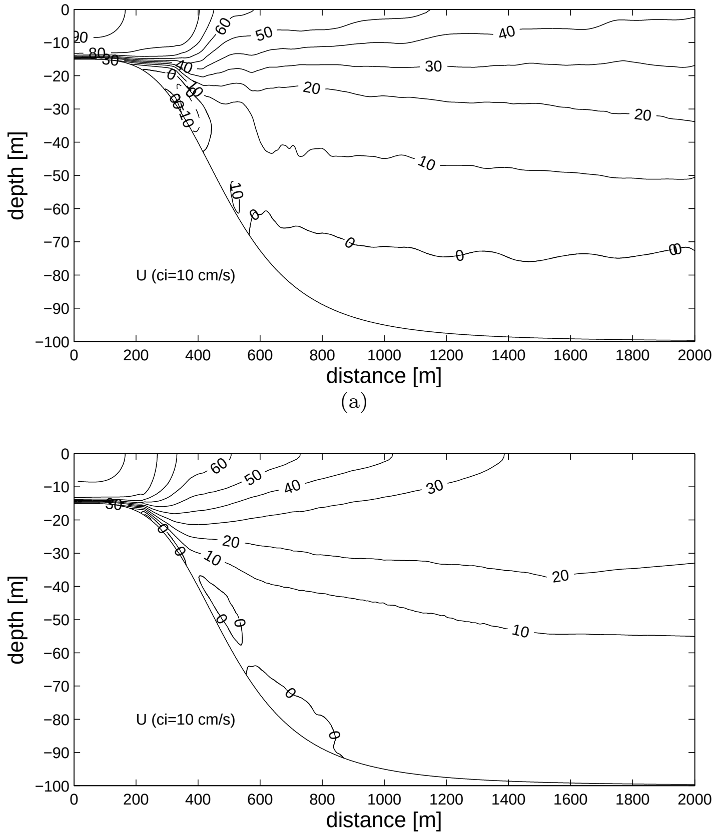

(a)

(b)

Fig. 12 The time mean horizontal velocity field for the non-hydrostatic experiment with small values of viscosity and diffusivity and $\Delta x = 1.5625\,\mathrm{m}$ (top figure), and the corresponding velocity field for the hydrostatic experiment in the bottom figure.

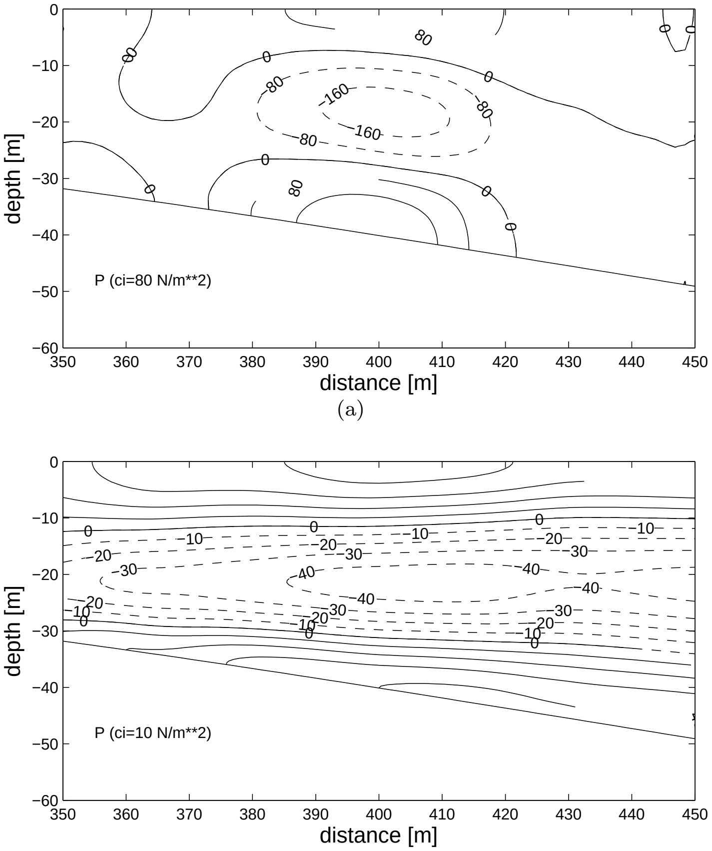

(a)

(b)

Fig. 13 The non-hydrostatic pressure field P_{NH} in the lee of the sill near the top for $\Delta x = 1.5625\,\mathrm{m}$ for the non-hydrostatic experiment with small values of viscosity and diffusivity. Negative pressures are indicated with dashed lines. The field after 1/4 T is given in a) and the time mean non-hydrostatic pressure field is given in b) .

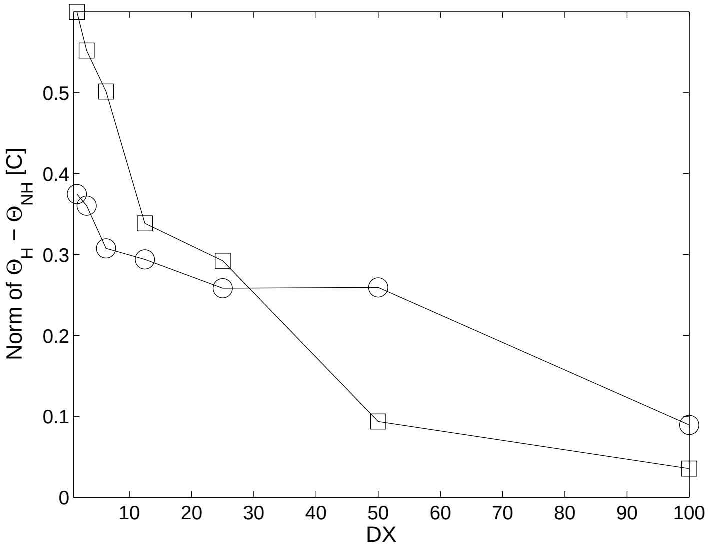

(a)

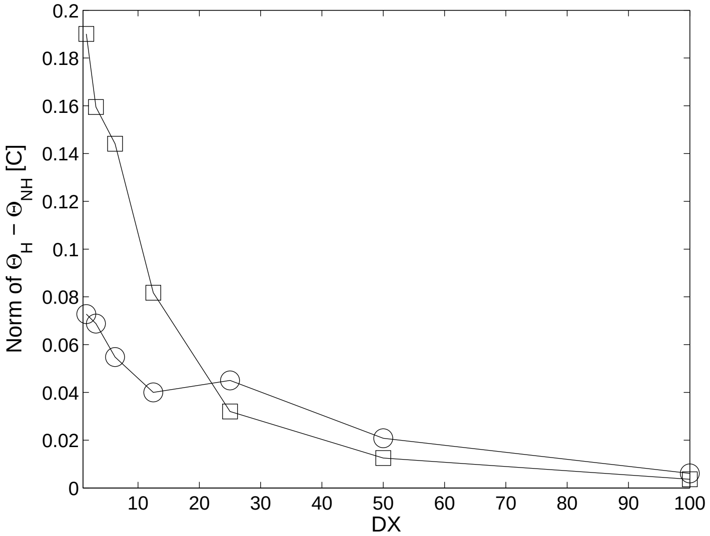

(b)

Fig. 14 The norms of the differences between the instantaneous temperature fields after 1/4 T produced with the non-hydrostatic model and the corresponding field produced with the hydrostatic model, see Equation 8, are given in the top figure as functions of Δx. The results for the experiments with large values of viscosity and diffusivity are given with circles and the results for the experiments with small values of viscosity and diffusivity are given with squares. The norms of the corresponding differences between the time mean temperature fields, see Equation 9, are given in the bottom figure.

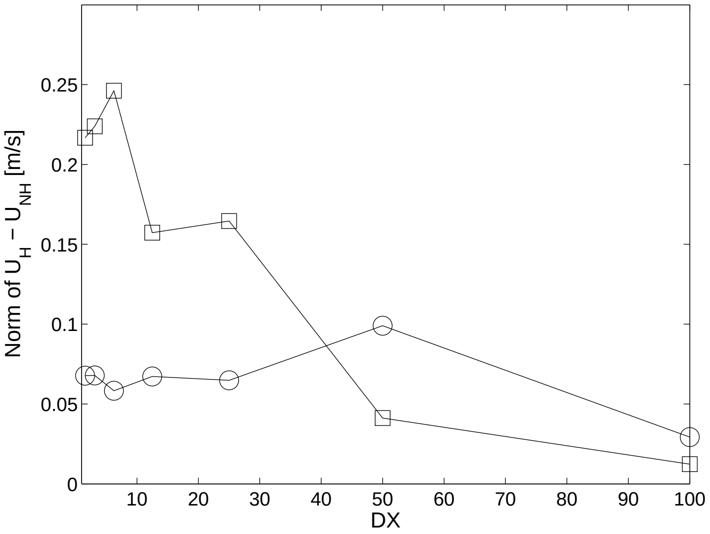

(a)

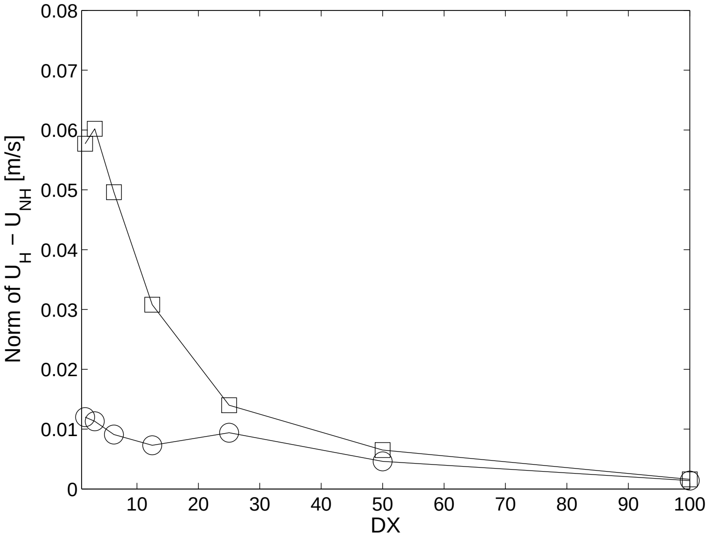

(b)

Fig. 15 The norms of the differences between the instantaneous horizontal velocity fields after 1/4 T produced with the non-hydrostatic model and the corresponding field produced with the hydrostatic model, see Equation 8, are given in the top figure as functions of Δx. The results for the experiments with large values of viscosity and diffusivity are given with circles and the results for the experiments with small values of viscosity and diffusivity are given with squares. The norms of the corresponding differences between the time mean horizontal velocity fields, see Equation 9, are given in the bottom figure.

References

Adcroft, A., Hill, C., and Marshall, J. (1999). A New Treatment of the Coriolis Terms in C-Grid Models at Both High and Low Resolutions. *Monthly Weather Review*, 127:1928–1936.

Afanasyev, Y. and Peltier, W. (2001a). On breaking internal waves over the sill in Knight Inlet. *Proceedings of the Royal Society of London A*, 457:2799–2825.

Afanasyev, Y. and Peltier, W. (2001b). Reply to comment on the paper 'On breaking internal waves over the sill in Knight Inlet'. *Proceedings of the Royal Society of London A*, 457:2831–2834.

Armi, L. and Farmer, D. (2002). Stratified flow over topography: bifurcation fronts and transition to the uncontrolled state. *Proceedings of the Royal Society of London A*, 458:513–538.

Avlesen, H., Berntsen, J., and Espelid, T. (2001). A convergence study of two prognostic, sigma coordinate ocean models on a density driven flow in a quadratic basin. *International Journal of Numerical Methods in Fluids*, 36:639–657.

Berntsen, H., Kowalik, Z., Sælid, S., and Sørli, K. (1981). Efficient numerical simulation of ocean hydrodynamics by a splitting procedure. *Modeling, Identification and Control*, 2:181–199.

Berntsen, J. (2000). USERS GUIDE for a modesplit σ-coordinate numerical ocean model. Technical Report 135, Dept. of Applied Mathematics, University of Bergen, Johs. Bruns gt.12, N-5008 Bergen, Norway. 48p.

Berntsen, J., Aksnes, D., and Foldvik, A. (2002). Production enhancement by artificial upwelling: a simulation study. *Hydrobiologia*, 484:177–190.

Berntsen, J. and Furnes, G. (2005). Internal pressure errors in sigma-coordinate ocean models- sensitivity of the growth of the flow to the time stepping method and possible non-hydrostatic effects. *Continental Shelf Research*, 25:829–848.

Berntsen, J., Xing, J., and Alendal, G. (2006). Assessment of non-hydrostatic ocean models using laboratory scale problems. *Continental Shelf Research*, 26:1433–1447.

Berntsen, J., Xing, J., and Davies, A. (2008). Numerical studies of internal waves at a sill: sensitivity to horizontal size and subgrid scale closure. *Continental Shelf Research*, 28:1376–1393.

Blumberg, A. and Mellor, G. (1987). A description of a three-dimensional coastal ocean circulation model. In Heaps, N., editor, *Three-Dimensional Coastal Ocean Models*, volume 4 of *Coastal and Estuarine Series*, pages 1–16. American Geophysical Union.

Carnevale, G., Briscolini, M., and Orlandi, P. (2001). Buoyancy- to inertial-range transition in forced stratified turbulence. *Journal of Fluid Mechanics*, 427:205–239.

Cummins, P. (2000). Stratified flow over topography: time-dependent comparisons between model solutions and observations. *Dynamics of Atmospheres and Oceans*, 33:43–72.

Cummins, P., Vagle, S., Armi, L., and Farmer, D. (2003). Stratified flow over topography: upstream influence and generation of nonlinear waves. *Proceedings of the Royal Society of London A*, 459:1467–1487.

Cushman-Roisin, B. (1994). *Introduction to Geophysical Fluid Dynamics*. Prentice Hall. ISBN-0-13-353301-8.

Davies, A. and Xing, J. (2007). On the influence of stratification and tidal forcing upon mixing in sill regions. *Ocean Dynamics*, 57:431–451.

Dörnbrack, A. (1998). Turbulent mixing by breaking gravity waves. *Journal of Fluid Mechanics*, 375:113–141.

Farmer, D. and Armi, L. (1999). Stratified flow over topography: The role of small-scale entrainment and mixing in flow establishment. *Proceedings of the Royal Society of London*, A455:3221–3258.

Farmer, D. and Armi, L. (2001). Stratified flow over topography: models versus observations . *Proceedings of the Royal Society of London A*, 457:2827–2830.

Farmer, D. and Freeland, H. (1983). The physical oceanography of fjords. *Progress in Oceanography*, 12:147–220.

Fringer, O. (2009). Towards Nonhydrostatic Ocean Modeling with Large-eddy Simulation. In Glickson, D., editor, *Oceanography in 2025: Proceedings of a Workshop*, pages 81–83. National Academic Press.

Fringer, O. and Street, R. (2003). The dynamics of breaking progressive interfacial waves. *Journal of Fluid Mechanics*, 494:319–353.

Griffies, S. (2004). *Fundamentals of Ocean Climate Models.* Princeton University Press.

Haidvogel, D. and Beckmann, A. (1999). *Numerical ocean circulation modeling*, volume 2 of *Series on Environmental Science and Management.* Imperial College Press.

Haney, R. (1991). On the pressure gradient force over steep topography in sigma coordinate ocean models. *Journal of Physical Oceanography*, 21:610–619.

Heggelund, Y., Vikebø, F., Berntsen, J., and Furnes, G. (2004). Hydrostatic and non-hydrostatic studies of gravitational adjustment over a slope. *Continental Shelf Research*, 24:2133–2148.

Hodges, B., Laval, B., and Wadzuk, B. (2006). Numerical error assessment and a temporal horizon for internal waves in a hydrostatic model. *Ocean Modelling*, 13:44–64.

Inall, M., Cottier, F., Griffiths, C., and Rippeth, T. (2004). Sill dynamics and energy transformation in a jet fjord. *Ocean Dynamics*, 54:307–314.

Inall, M., Rippeth, T., Griffiths, C., and Wiles, P. (2005). Evolution and distribution of TKE production and dissipation within stratified flow over topography. *Geophysical Research Letters*, 32:L08607,doi:10.1029/2004GL022289.

Kanarska, Y. and Maderich, V. (2003). A non-hydrostatic numerical model for calculating free-surface stratified flows. *Ocean Dynamics*, 53:176–185, doi:10.1007/s10236–003–0039–6.

Kanarska, Y., Shchepetkin, A., and McWilliams, J. (2007). Algorithm for non-hydrostatic dynamics in the Regional Oceanic Modeling System. *Ocean Modelling*, 18:143–174.

Kantha, L. and Clayson, C. (2000). *Numerical models of oceans and oceanic processes.* International Geophysics Series Volume 66. Academic Press.

Klymak, J. and Gregg, M. (2001). Three-dimensional nature of flow near a sill . *Journal of Geophysical Research*, 106:22295–22311.

Klymak, J. and Gregg, M. (2003). The Role of Upstream Waves and a Downstream Density Pool in the Growth of Lee Waves:Stratified Flow over the Knight Inlet Sill. *Journal of Physical Oceanography*, 33:1446–1461.

Klymak, J. and Gregg, M. (2004). Tidally Generated Turbulence over the Knight Inlet Sill. *Journal of Physical Oceanography*, 34:1135–1151.

Kowalik, Z. and Murty, T. (1993). *Numerical Modeling of Ocean Dynamics*, volume 5 of *Advanced Series on Ocean Engineering*. World Scientific.

Kundu, P. and Cohen, I. (2008). *Fluid Mechanics*. Elsevier Academic Press.

Kunze, E. and Llewellyn Smith, S. (2004). The Role of Small-Scale Topography in Turbulent Mixing of the Global Ocean. *Oceanography*, 17:55–64.

Lamb, K. (2004). On boundary-layer separation and internal wave generation at the Knight Inlet sill. *Proceedings of the Royal Society of London A*, 460:2305–2337.

Lamb, K. (2007). Energy and Pseudoenergy Flux in the Internal Wave Field Generated by Tidal Flow over Topography. *Continental Shelf Research*, 27:1208–1232.

Legg, S. and Adcroft, A. (2003). Internal wave breaking at concave and convex continental slopes. *Journal of Physical Oceanography*, 33:2224–2246.

Marshall, J., Adcroft, A., Hill, C., Perelman, L., and Heisey, C. (1997a). A finite-volume, incompressible Navier Stokes model for studies of the ocean on parallel computers. *Journal of Geophysical Research*, 102(C3):5753–5766.

Marshall, J., Hill, C., Perelman, L., and Adcroft, A. (1997b). Hydrostatic, quasi-hydrostatic, and nonhydrostatic ocean modeling. *Journal of Geophysical Research*, 102(C3):5733–5752.

Martinsen, E. and Engedahl, H. (1987). Implementation and testing of a lateral boundary scheme as an open boundary condition in a barotropic ocean model. *Coastal Engineering*, 11:603–627.

Mellor, G. (1996). Users guide for a three-dimensional, primitive equation, numerical ocean model. Technical report, Princeton University.

Mellor, G., Oey, L.-Y., and Ezer, T. (1998). Sigma coordinate pressure gradient errors and the seamount problem. *Journal of Atmospheric and Oceanic Technology*, 15:1122–1131.

Munk, W. and Wunsch, C. (1998). Abyssal recipes II: energetics of tidal and wind mixing. *Deep-Sea Research I*, 45:1978–2010.

Polzin, K., Toole, J., Ledwell, J., and Schmitt, R. (1997). Spatial variability of turbulent mixing in the abyssal ocean. *Science*, 276:93–96.

Rickard, G., O'Callaghan, J., and Popinet, S. (2009). Numerical simulations of internal solitary waves interacting with uniform slopes using an adaptive model. *Ocean Modelling*, 30:16–28.

Samelson, R. (1998). Large scale circulation with locally enhanced vertical mixing. *Journal of Physical Oceanography*, 28:712–726.

Smyth, W., Nash, J., and Moum, J. (2005). Differential Diffusion in Breaking Kelvin-Helmholtz Billows. *Journal of Physical Oceanography*, 35:1004–1022.

Spall, M. (2001). Large-scale circulations forced by localized mixing over a sloping bottom. *Journal of Physical Oceanography*, 31:2369–2384.

Stacey, M. (1985). Some Aspects of the Internal Tide in Knight Inlet, British Columbia . *Journal of Physical Oceanography*, 15:1652–1661.

Stacey, M. and Gratton, Y. (2001). The Energetics and Tidally Induced Reverse Renewal in a Two-Silled Fjord. *Journal of Physical Oceanography*, 31:1599–1615.

Stashchuk, N., Inall, M., and Vlasenko, V. (2007). Analysis of Supercritical Stratified Tidal Flow in a Scottish Fjord . *Journal of Physical Oceanography*, 37:1793–1810.

Stigebrandt, A. (1976). Vertical diffusion driven by internal waves in a sill fjord. *Journal of Physical Oceanography*, 6:486–495.

Stigebrandt, A. (1999). Resistance to barotropic tidal flow in straits by baroclinic wave drag. *Journal of Physical Oceanography*, 29:191–197.

Stigebrandt, A. and Aure, J. (1989). Vertical Mixing in Basin Waters of Fjords. *Journal of Physical Oceanography*, 19:917–926.

Vlasenko, V., Stashchuk, N., and Hutter, K. (2002). Water exchange in fjords induced by tidally generated internal lee waves. *Dynamics of Atmospheres and Oceans*, 35:63–89.

Wadzuk, B. and Hodges, B. (2004). Hydrostatic and Non-hydrostatic Internal Wave models. Technical Report CRWR Online Report 04-09, University of Texas at Austin.

Wunsch, C. (1970). On oceanic boundary mixing. *Deep-Sea Research*, 17:293–301.

Wunsch, C. and Ferrari, R. (2004). Vertical Mixing, Energy, and the General Circulation of the Oceans. *Annual Review of Fluid Mechanics*, 36:281–314.

Xing, J. and Davies, A. (2001). A three-dimensional baroclinic model of the Irish Sea: Formation of the thermal fronts and associated circulation. *Journal of Physical Oceanography*, 31:94–114.

Xing, J. and Davies, A. (2006a). Processes influencing tidal mixing in the region of sills. *Geophysical Research Letters*, 33:L04603 doi:10.1029/2005GL025226.

Xing, J. and Davies, A. (2006b). Influence of stratification and topography upon internal wave spectra in the region of sills. *Geophysical Research Letters*, 33:L23606 doi:10.1029/2005GL025226.

Xing, J. and Davies, A. (2007). On the importance of non-hydrostatic processes in determining tidally induced mixing in sill regions. *Continental Shelf Research*, 27:2162–2185.

Yang, H. and Przekwas, A. (1992). A comparative study of advanced shock-capturing schemes applied to Burgers equation. *Journal of Computational Physics*, 102:139–159.